Journal of Sol-Gel Science and Technology (2024) 110:156–168
https://doi.org/10.1007/s10971-024-06353-5

ORIGINAL PAPER

Development and application of multifunctional $Fe_3O_4/SiO_2/TiO_2/Cu$ nanocomposites for sustainable water treatment

Mohammad-Peyman Mazhari[1] · Hossein Khojasteh[1] · Nowjuan Sharifi[2] · Peyman Aspoukeh[1] · Seyed Mahdi Mousavi[3]

Received: 26 December 2023 / Accepted: 19 February 2024 / Published online: 2 March 2024

Abstract

This investigation entailed the synthesis of $Fe_3O_4/SiO_2/TiO_2$ via the sol-gel technique, and the $Fe_3O_4/SiO_2/TiO_2/Cu$ nanocomposite utilizing $Cu(NO_3)_2.3H_2O$ through the photodeposition approach. Subsequent to synthesis, these specimens underwent comprehensive characterization employing an array of analytical techniques, including X-ray diffraction (XRD), scanning electron microscopy (SEM), energy dispersive X-ray microanalysis (EDS), vibrating sample magnetometry (VSM), Diffuse Reflectance Spectroscopy (DRS) and Fourier transform infrared (FT-IR) spectroscopy. The focal point of this study was the assessment of the catalytic proficiency of both $Fe_3O_4/SiO_2/TiO_2$ and $Fe_3O_4/SiO_2/TiO_2/Cu$ magnetically responsive nanocatalysts in facilitating the degradation of Reactive Methylene Blue (MB) under ultraviolet irradiation at ambient temperature. A notable attribute of these magnetic nanocomposites is their capacity for complete recovery, enabled by the application of an external magnetic field, thereby demonstrating significant potential for practical applications in environmental remediation.

Graphical Abstract

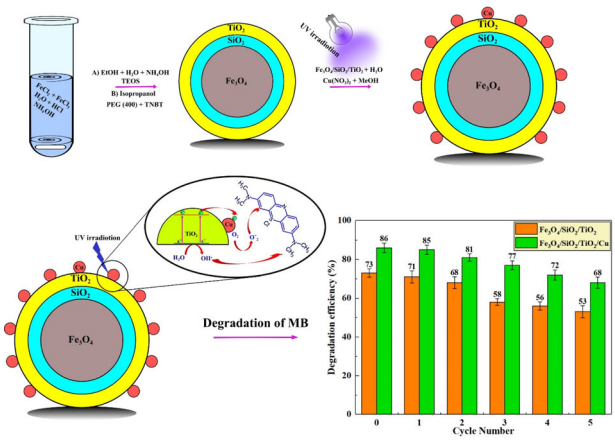

Keywords Nanocomposites · Photocatalysis · $Fe_3O_4/SiO_2/TiO_2/Cu$ · Sol-gel method · Photodeposition · Magnetic Separation

✉ Hossein Khojasteh
hossein.ahmed@soran.edu.iq

[1] Department of Nanotechnology, Scientific Research Center, Soran University, Soran, Kurdistan Region, Iraq

[2] Department of Chemistry, University of Kurdistan, Sanandaj, Iran

[3] Department of Applied Chemistry, Faculty of Chemistry, University of Kashan, Kashan, Iran

Highlights

- A combination of sol-gel and photodeposition method was developed for the fabrication of $Fe_3O_4/SiO_2/TiO_2/Cu$ nanocomposites, showcasing a breakthrough in materials science for water treatment technologies.
- The study demonstrates a significant improvement in the degradation of methylene blue dye under UV light, marking a pivotal advancement in the effectiveness of water purification methods.
- The easy magnetic recovery feature of the nanocomposites was highlighted, enabling their efficient reuse and contributing to waste reduction in water treatment processes.
- The research unveils the synergistic effects between TiO_2 and Cu, enhancing photocatalytic activity and leading to faster degradation rates, which underscores the importance of component interaction in nanocomposites.
- The potential of these nanocomposites to address environmental pollution was emphasized, offering a novel, reusable, and efficient solution for water purification, highlighting the article's contribution to sustainable environmental management.

1 Introduction

The burgeoning issue of water pollution, particularly stemming from dye wastewater, has escalated into a grave environmental concern in recent years. A diverse array of methodologies has been employed to mitigate this challenge, encompassing techniques such as membrane processes [1], photocatalytic degradation [2–4], and a combination of biological and physicochemical treatments [5, 6]. Among these, heterogeneous photocatalysts have emerged as one of the most efficacious approaches. This is attributed to their numerous advantageous properties, including non-toxicity, high efficiency, cost-effectiveness, stability, widespread availability, and the potential for recycling in the realm of wastewater treatment [7–10].

Various support structures, including dendrimers, polymers, and ligands, have been successfully employed as substrates for nanocatalysts [11]. A primary challenge associated with the utilization of nanoparticles as catalyst supports lies in their intricate separation and recycling processes [12]. To address this issue, certain magnetic nanoparticles, such as Fe_3O_4, $ZnFe_2O_4$, and $CoFe_2O_4$, have been adopted either as a core or as a support mechanism for the immobilization of other nanocatalysts. The utilization of magnetic separation techniques facilitates the recovery and rejuvenation of these magnetic materials through the application of external magnetic fields [13, 14]. Moreover, the incorporation of a magnetic core not only aids in separation but also contributes to an increase in surface area, which can significantly enhance photocatalytic activity [15, 16].

One of the predominant drawbacks inherent in semiconductor photocatalysis is the propensity for the recombination of photogenerated electrons (e^-) and holes (h^+), a phenomenon that culminates in the dissipation of energy and the consequent diminution of photocatalytic yields. This process of carrier generation and recombination transpires as electrons transition from the valence band to the conduction band within a semiconductor, an event that may occur due to interactions with other electrons, holes, photons, or even the vibrational dynamics of the crystal lattice itself [17]. To circumvent this reduction in efficiency, it is imperative to strategize against the recombination of these electrons and holes. In this context, the employment of coupled semiconductors has been identified as a viable approach to augment charge separation of electron-hole pairs. This strategy effectively extends the lifespan of both electrons and holes, thereby substantially mitigating the recombination of charge carriers [18–21]. The ultimate outcome of this approach is a marked enhancement in the efficiency of the photocatalyst [22, 23].

The field of semiconductor photocatalysis has gained significant momentum due to its potential in addressing environmental pollution, particularly in the degradation of organic pollutants in wastewater. This technology hinges on the unique properties of semiconductors to catalyze reactions under light irradiation. The effectiveness of these photocatalysts, however, is not without its challenges, particularly in the realm of charge carrier recombination, as previously discussed [24, 25].

Recent advancements in nanotechnology have opened new avenues in the design and synthesis of more efficient photocatalysts. Nanocatalysts, due to their nanoscale dimensions, exhibit enhanced surface-to-volume ratios, leading to increased reaction sites and improved catalytic activity [26]. Furthermore, the integration of nanotechnology in photocatalysis has facilitated the development of novel materials with tailored band gaps, allowing for the absorption of a broader spectrum of light, including visible and near-infrared regions [27].

Another critical area in semiconductor photocatalysis is the development of sustainable and eco-friendly photocatalytic materials. As global environmental concerns escalate, the focus has shifted towards materials that are not only efficient but also environmentally benign. This has led to the exploration of biocompatible and non-toxic materials in the synthesis of photocatalysts [28].

The application of photocatalysis extends beyond wastewater treatment. It has shown promise in the fields of

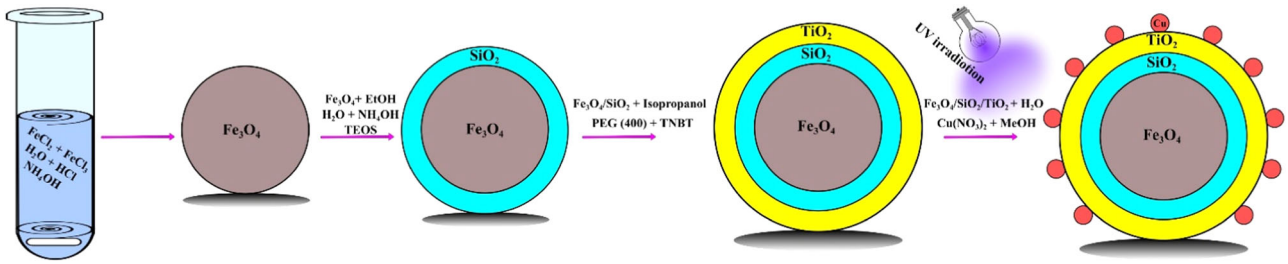

Scheme 1 Schematic illustration of the synthesis of $Fe_3O_4/SiO_2/TiO_2/Cu$ nanoparticles

hydrogen production through water splitting, CO_2 reduction, and even in the air purification process. These applications demonstrate the versatility and potential of photocatalysis in contributing to a sustainable and cleaner environment [29, 30].

In summary, while semiconductor photocatalysis presents a promising solution to environmental pollution, ongoing research and development are essential to overcome existing limitations and realize its full potential. The integration of nanotechnology and the focus on sustainable practices are critical in advancing this field further [31, 32].

In the present study, the synthesis of $Fe_3O_4/SiO_2/TiO_2$ was initially conducted employing the sol-gel method, followed by the fabrication of the $Fe_3O_4/SiO_2/TiO_2/Cu$ nanocomposite via the photodeposition technique. The photocatalytic activities of both $Fe_3O_4/SiO_2/TiO_2$ and $Fe_3O_4/SiO_2/TiO_2/Cu$ were rigorously evaluated, employing methylene blue dye as a model organic compound to assess their efficacy. Furthermore, the recovery attributes of the catalysts were meticulously examined under the influence of an external magnetic field. This analysis was extended to investigate the catalytic properties post-recycling, following multiple usage cycles.

The intricate growth process of the composite nanoparticles is elucidated in Scheme 1. The scheme reflects the sequential layer-by-layer deposition of different materials. Each layer contributes unique properties to the final nanocomposite, such as magnetic properties from Fe_3O_4, stability and surface functionality from SiO_2, photocatalytic activity from TiO_2, and enhanced catalytic performance from Cu.

2 Experimental

2.1 Materials and methods

The chemicals used in this study, all sourced from Merck Company, include Iron (II) chloride hydrate, 98% purity; Iron (III) chloride hydrate, 97% purity; Copper(II) nitrate trihydrate ($Cu(NO_3)_2{\cdot}3H_2O$), 97% purity; Tetraethyl orthosilicate (TEOS), 95% purity; Tetra-n-butyl titanate (TNBT), 98% purity; aqueous ammonia solution, 32% purity; hydrochloric acid, 38% purity; Polyethylene glycol 400 (PEG 400), 90% purity; ethanol, 99% purity; methanol, 99% purity; and acetylacetone, 97% purity. These reagents were employed in their original state without any additional purification. Methylene Blue (MB), possessing the chemical formula $C_{16}H_{18}ClN_3S$, was procured from Alvan Co., Iran. Throughout the sample preparation process, deionized water was utilized exclusively.

X-ray diffraction (XRD) patterns were acquired using a Philips X-ray diffractometer, equipped with Ni-filtered Cu Kα radiation. The morphological characteristics and size distribution of the nanomaterials were determined using a Scanning Electron Microscope (SEM) (Philips XL-30ESM). Fourier Transform Infrared (FT-IR) spectra of the samples were recorded utilizing a Nicolet Magna IR 550 spectrometer. Magnetic measurements were conducted at room temperature employing a Vibrating Sample Magnetometer (VSM) (BHV-55, Riken, Japan). UV–Visible absorption spectra were obtained with a UV–Visible spectrophotometer (Perkin Elmer Lambda2S, Germany) in the wavelength range of 200 to 800 nm.

2.2 Preparation of Fe_3O_4/SiO_2 nanoparticles

The Fe_3O_4 magnetic nanoparticles were synthesized employing a co-precipitation technique. Initially, Iron(III) chloride hexahydrate ($FeCl_3.6H_2O$, 3.88 g) and Iron(II) chloride tetrahydrate ($FeCl_2{\cdot}4H_2O$, 1.431 g) were dissolved in 30 mL of 0.4 M hydrochloric acid (HCl), maintaining a molar ratio of 2:1. Subsequently, 120 mL of 25% NH_4OH, which had been previously degassed, was incrementally added to this solution while stirring in an ultrasound bath. The addition of the base resulted in the immediate formation of a black precipitate. This precipitate was subjected to continuous stirring in the ultrasound bath for an additional 20 min. The magnetic nanoparticles were then separated using a magnet and subsequently washed thrice with ethanol and distilled water [33].

In order to mitigate the susceptibility of the Fe_3O_4 magnetic nanoparticles to heat and oxidation, a protective layer of SiO_2 was applied. For this coating process, 0.4 g of

the synthesized Fe_3O_4 was dispersed in 150 mL of ethanol, to which 40 mL of deionized water and 2 mL of ammonium hydroxide were added. This dispersion was sonicated for 45 min. Thereafter, 4 mL of TEOS was gradually introduced into the mixture. The solution was then stirred at room temperature for 3 h. Following this, the Fe_3O_4/SiO_2 particles were isolated and washed thrice, alternating between ethanol and water for each wash.

2.3 Synthesis of $Fe_3O_4/SiO_2/TiO_2$ nanocomposite

The $Fe_3O_4/SiO_2/TiO_2$ nanocomposite was synthesized utilizing the sol-gel method. Initially, 0.9 g of Fe_3O_4/SiO_2 nanoparticles were dispersed in 100 ml of 2-Propanol, followed by sonication for a duration of 30 min. Subsequently, 8 ml of Polyethylene glycol 400 (PEG 400) was incorporated into this mixture. In a separate container, a solution was prepared by adding 5 ml of TNBT and 1 ml of acetylacetone to 15 ml of 2-Propanol. This solution was stirred using a magnetic stirrer for 20 min to ensure homogeneity. This solution was then gradually introduced into the previously prepared nanoparticle mixture, with continuous stirring on the magnetic stirrer.

Upon completion of the addition, 5 ml of deionized water was added to the mixture. The resulting mixture was then stirred at a temperature of 60 °C for 10 h. Post-stirring, the gray precipitate that formed was separated using a magnet and subsequently washed with ethanol and deionized water. The washed precipitate was then dried at a temperature of 70 °C. The final step involved calcining the dried product in air at a temperature of 450 °C for 2 h, completing the synthesis process of the $Fe_3O_4/SiO_2/TiO_2$ nanocomposite.

2.4 Synthesis of $Fe_3O_4/SiO_2/TiO_2/Cu$ nanocatalyst

The $Fe_3O_4/SiO_2/TiO_2/Cu$ nanoparticles were synthesized employing the photodeposition method. Initially, Copper(II) nitrate trihydrate ($Cu(NO_3)_2.3H_2O$) weighing 0.00604 g was dissolved in 50 ml of deionized water to prepare a 0.5 mM solution. Subsequently, 0.1 g of the pre-synthesized $Fe_3O_4/SiO_2/TiO_2$ nanoparticles was added to this copper nitrate solution. This mixture was then stirred using a magnetic stirrer for a duration of 30 min, after which 0.5 ml of methanol (sourced from Merck) was added to the solution. The resulting mixture was transferred to a quartz tube and subjected to continuous stirring under UV irradiation for a period of 12 h.

Upon completion of the irradiation process, the product was isolated using an external magnetic field. The separated nanoparticles were then thoroughly washed three times, alternating between deionized water and ethanol. Finally, the washed nanoparticles were dried at a temperature of 60 °C for 12 h, culminating in the successful synthesis of $Fe_3O_4/SiO_2/TiO_2/Cu$ nanoparticles. Scheme 1 illustrates the methodical deposition of materials in a layer-by-layer sequence.

2.5 Assessment of photocatalytic activity of $Fe_3O_4/SiO_2/TiO_2/Cu$ nanocatalyst

The photocatalytic efficacy of the synthesized $Fe_3O_4/SiO_2/TiO_2/Cu$ nanocatalyst was evaluated through the photodegradation of MB aqueous solution, a model water pollutant. The experiment was conducted in a 100 ml quartz reaction tube. The reaction mixture was composed of the photocatalyst (50 mg) and an MB solution (10 mg L^{-1}), ensuring the availability of oxygen for the reaction. The mixture was continuously stirred using a magnetic stirrer.

In the experimental setup, the quartz tube within the photoreactor was carefully positioned at a distance of 40 cm from the UV light source. During the reaction, which involved UV lamp irradiation, the reaction mixture in the vessel was maintained at this same distance from a 200 W Mercury UV lamp, ensuring optimal exposure and efficiency of the photocatalytic process. Prior to irradiation, the solution was stirred in the dark for 20 min to establish equilibrium. The photodegradation process was monitored by measuring the concentration variation of MB over time, utilizing UV-Visible absorbance spectra.

3 Results and discussion

The crystalline phase and purity of the synthesized magnetic nanoparticles were characterized by XRD. The XRD pattern of the Fe_3O_4 nanoparticles, depicted in Fig. 1a, exhibits six prominent diffraction peaks at 2θ values of 30.76°, 36°, 43.91°, 54.27°, 58°, and 63.46°. This spectrum shows distinct peaks that can be indexed to Fe_3O_4, which is magnetite. The peaks are sharp and well-defined, indicating good crystallinity of the material. The characteristic peaks of Fe_3O_4 are designated with delta (Δ) symbols which are indicative of the crystalline structure of Fe_3O_4 magnetic nanostructures.

Figure 1b presents the XRD pattern of the $Fe_3O_4/SiO_2/TiO_2$ magnetic nanoparticles. In this spectrum, along with the peaks corresponding to Fe_3O_4, additional peaks appear that can be attributed to SiO_2 (marked with asterisks) and TiO_2 (marked with triangles). The presence of these peaks suggests the successful formation of a composite material. The SiO_2 peaks are less sharp, which could indicate a lower crystallinity or smaller particle size of the silica component. This broad peak centered at a 2θ value of approximately 23° is observed, which is characteristic of amorphous SiO_2, suggesting the presence of a non-crystalline SiO_2 shell coating. Additionally, distinct peaks at 2θ values of 24.45°,

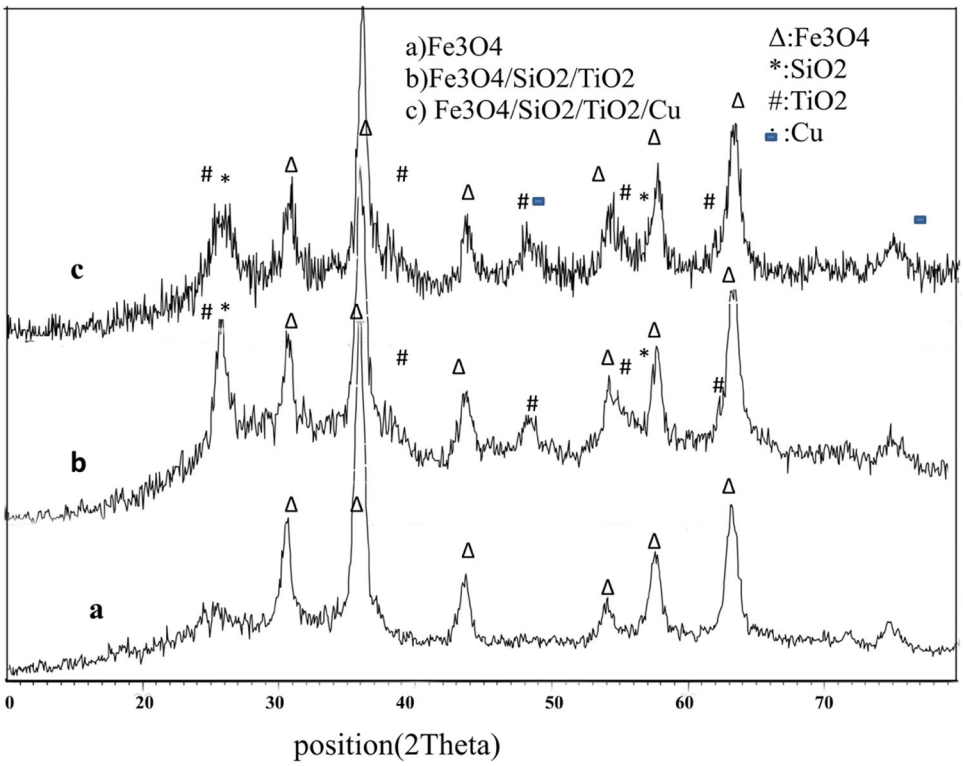

Fig. 1 XRD patterns of (**a**) Fe_3O_4, (**b**) $Fe_3O_4/SiO_2/TiO_2$ and (**c**) $Fe_3O_4/SiO_2/TiO_2$/Cu nanoparticles

37.57°, and 46.3° confirm the anatase phase of TiO_2, integrated within the composite. The TiO_2 peaks correspond to the anatase phase of TiO_2, which is commonly used for photocatalysis.

The XRD pattern for the $Fe_3O_4/SiO_2/TiO_2$/Cu nanocatalyst, illustrated in Fig. 1c, reveals that due to the minimal loading of Cu on the magnetic nanoparticles, the diffraction peak corresponding to Cu is of low intensity. This spectrum includes all the peaks seen in sample b, with the addition of new peaks that can be indexed to metallic copper (Cu), indicated by filled squares. This suggests the presence of Cu in the nanocomposite, albeit in a small quantity that does not significantly alter the overall crystalline structure observed in the XRD pattern. This suggests that Cu nanoparticles have been successfully deposited onto the surface of the $Fe_3O_4/SiO_2/TiO_2$ composite.

The presence of metallic copper can be advantageous for photocatalytic applications as it may act as a co-catalyst to improve the efficiency of the photocatalytic process. The XRD analysis of $Fe_3O_4/SiO_2/TiO_2$/Cu nanocomposites provides critical insights into their structural and compositional attributes, which directly influence their photocatalytic efficiency in degrading organic pollutants like Methylene Blue dye. This analysis reveals a higher degree of crystallinity within the nanocomposites, indicative of fewer structural defects, thus facilitating efficient charge transfer and reduced recombination of electron-hole pairs, essential for photodegradation. Additionally, the XRD results suggest smaller particle sizes, leading to an increased surface area to volume ratio, which offers more active sites for the photocatalytic reactions and enhances the absorption of dye molecules, thereby improving the degradation efficiency under UV light. The identification of specific crystalline phases, particularly the presence of anatase and rutile phases in TiO_2, further underscores the nanocomposite's potential for high photocatalytic activity, with anatase known for its efficacy in photodegradation processes. Moreover, the XRD analysis hints at the synergistic effects between the different components of the nanocomposite, such as the interaction between TiO_2 and Cu, potentially creating a heterojunction that improves charge separation and hence, the overall photocatalytic efficiency.

The elemental composition and chemical purity of the $Fe_3O_4/SiO_2/TiO_2$/Cu sample were rigorously assessed utilizing Energy Dispersive X-ray Spectroscopy (EDS) (Fig. 2). The EDS spectrum of the $Fe_3O_4/SiO_2/TiO_2$/Cu sample reveals the elemental composition of the nanocomposite. A significant peak at ~0.5 KeV indicates a substantial oxygen presence, which is a common element in the oxides that comprise the sample. Silicon is clearly present, as evidenced by the distinct peaks around 1.7 KeV, confirming the silica component of the composite. Iron, a constituent of Fe_3O_4, manifests through multiple peaks observed near 0.7 KeV and in the 6–7 KeV range, corroborating the inclusion of iron oxide within the nanocomposite. Titanium's presence is validated by peaks at about 4.5 KeV, indicative of the

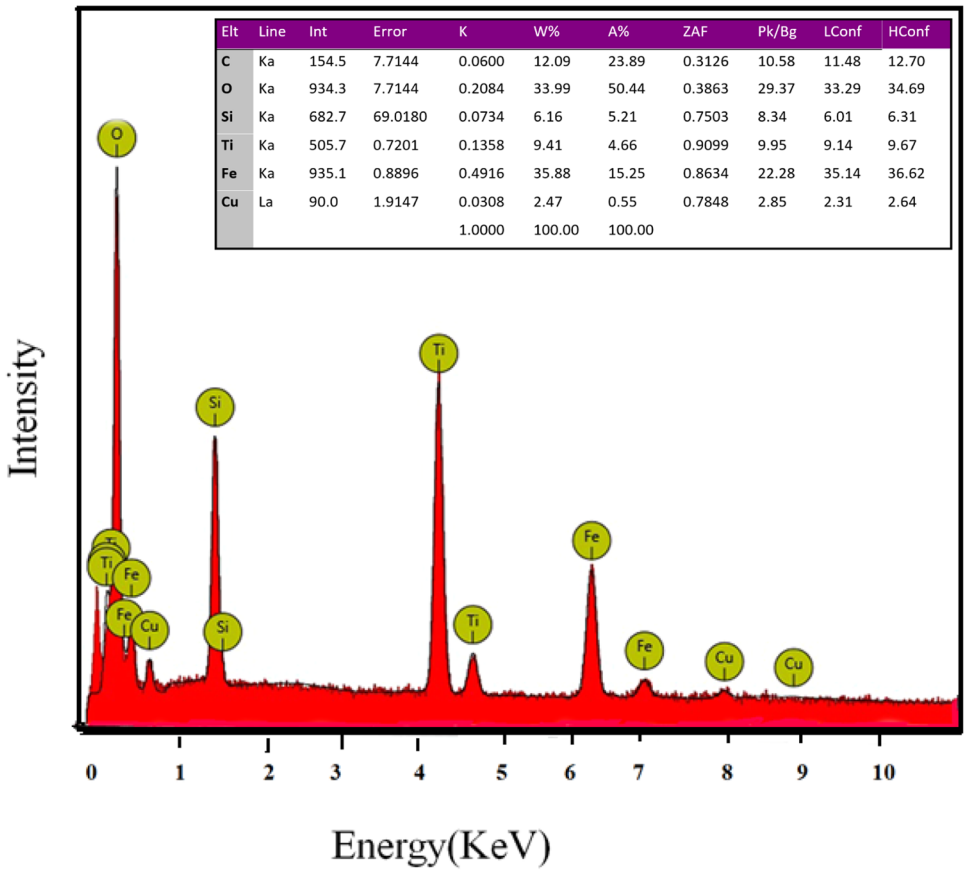

Fig. 2 Energy dispersive x-ray spectroscopy (EDS) analysis and the weight percentages of all components of the $Fe_3O_4/SiO_2/TiO_2$/Cu nanocomposite

titanium dioxide phase. Finally, copper, incorporated into the composite as Cu, is denoted by peaks just above 8 KeV. The absence of peaks for elements not expected in the sample suggests that the nanocomposite is relatively pure and consists primarily of the intended Fe_3O_4, SiO_2, TiO_2, and Cu components. The weight percentages (W%) for these elements are C: 12.09%, O: 33.99%, Si: 6.16%, Ti: 9.41%, Fe: 35.88%, and Cu: 2.47%. The presence of carbon is attributed to the conductive carbon fiber coating applied to the samples before electron microscopy to prevent charge accumulation. This coating is not part of the nanocomposite's intrinsic composition. The high percentage of iron reflects the Fe_3O_4 core, while Ti and Si percentages are consistent with the TiO_2 and SiO_2 layers, respectively, and Cu indicates the doping level within the composite. The EDS analysis, therefore, confirms the successful synthesis of the $Fe_3O_4/SiO_2/TiO_2$/Cu nanocomposite with a high degree of elemental purity.

The morphological characteristics of the samples were meticulously investigated using Scanning Electron Microscopy (SEM), as depicted in Fig. 3. The SEM image for Fe_3O_4 sample displays a uniform morphology with particles that appear to be consistent in size and shape (Fig. 3a). The surface seems relatively smooth, and the particles are closely packed, indicating good crystallinity and a high degree of aggregation.

Figure 3b displays SEM result for Fe_3O_4/SiO_2 sample. In this image, the Fe_3O_4 particles are encapsulated with a SiO_2 layer. While the underlying particle structure remains consistent, there is a slight increase in the apparent size due to the silica coating. The particles maintain a high level of uniformity, and the SiO_2 coating does not significantly disrupt the overall morphology.

The morphology of the $Fe_3O_4/SiO_2/TiO_2$, synthesized via the co-precipitation method, is showcased in Fig. 3c. This image shows that the addition of TiO_2 to the Fe_3O_4/SiO_2 composite results in a more complex surface structure. The particles retain their uniformity to some degree, but the introduction of TiO_2 brings about a noticeable change in the textural features, with some increase in the roughness of the particles.

Figure 3d illustrates the nanocomposite after the addition of copper. The SEM image reveals an increase in the roughness and size of the particles, which is consistent with the deposition of Cu on the surface. The particles appear to be agglomerated, and the copper coating contributes to a more heterogeneous and coarse surface morphology compared to the other samples.

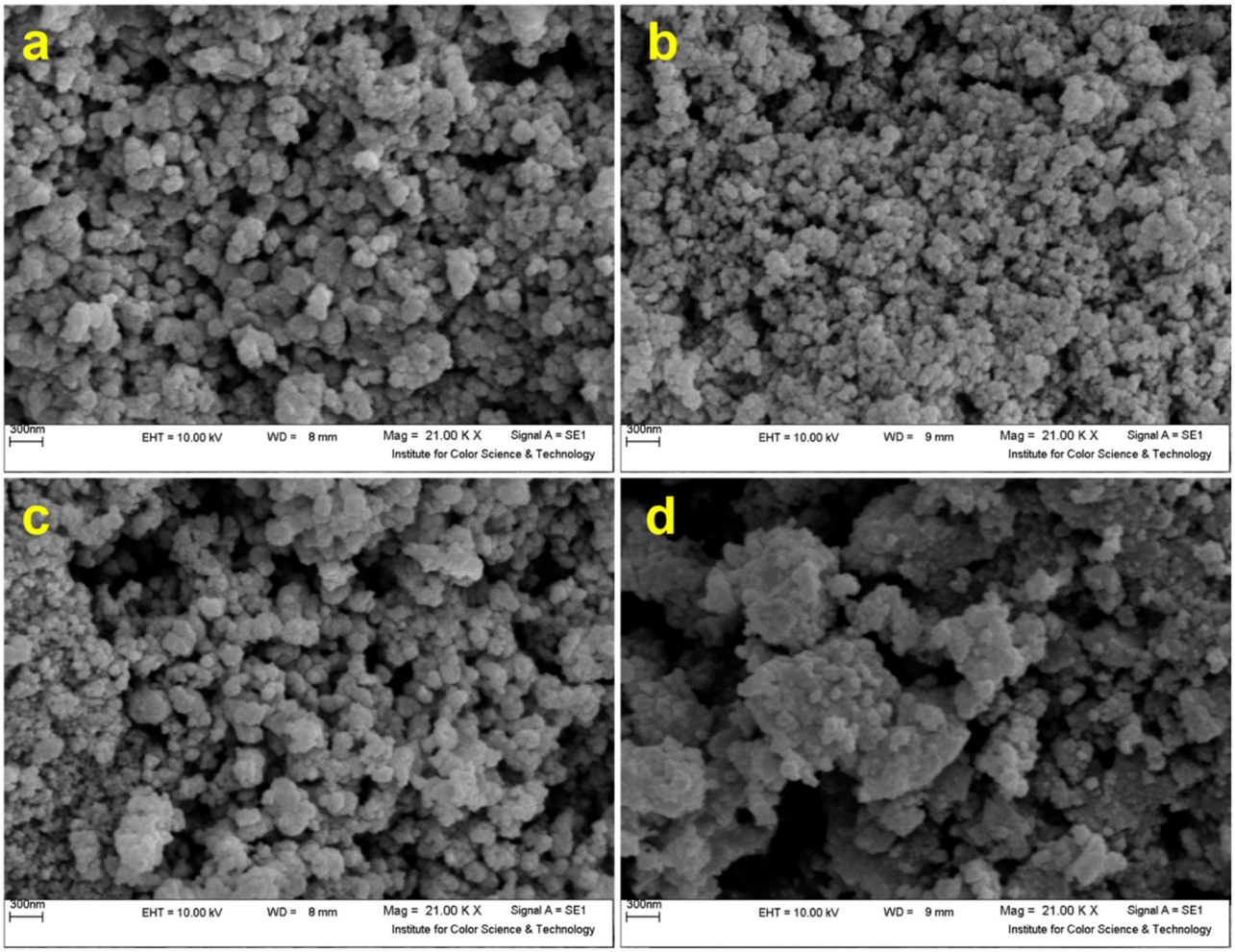

Fig. 3 SEM images of (**a**) Fe_3O_4, (**b**) Fe_3O_4/SiO_2, (**c**) $Fe_3O_4/SiO_2/TiO_2$ and (**d**) $Fe_3O_4/SiO_2/TiO_2/Cu$ nanocomposite

To ascertain the actual dimensions of the $Fe_3O_4/SiO_2/TiO_2/Cu$ nanocomposite, Transmission Electron Microscopy (TEM) was employed for analysis (Fig. 4). According to TEM images, there is a noticeable variation in contrast within the nanoparticles, which could indicate different materials or phases present within the composite. The darker areas could be the denser Fe_3O_4 or TiO_2 phases, while the lighter areas could be SiO_2. The scale bars help determine the size distribution of the nanoparticles. The images show a range of particle sizes, generally below 100 nm as indicated by the scale bar, which is typical for nanocomposites and desirable for certain applications like catalysis or sensing due to the large surface area to volume ratio. The findings suggest that the mean diameter of the nanocomposite particles is approximately 75 nanometers. There is a degree of aggregation visible, which is common for nanoparticles due to high surface energy leading to attractive forces between them. The morphology of the particles appears to be mostly spherical, with some degree of agglomeration which could affect the properties of the nanocomposite.

The FT-IR spectra presented in Fig. 5 elucidate the chemical structure of the synthesized samples. Specifically, the spectrum labeled Fig. 5a reveals a peak at 561 cm^{-1}, which can be assigned to the Fe–O stretching vibration, characteristic of iron oxide in the Fe_3O_4 nanoparticles [34, 35]. Across all samples, the consistent absorption band at approximately 1630 cm^{-1} is indicative of the bending vibrations of adsorbed water molecules [36, 37], while the broad absorption band between 3375 and 3432 cm^{-1} corresponds to the stretching vibrations of Si–O–H and the vibrations of residual hydroxyl groups on the surface of the silica-coated magnetic nanoparticles [38, 39]. In Fig. 5b, the peak at 1083 cm^{-1} is associated with Si–O stretching vibrations [39], and the broad bands appearing in the 530–600 cm^{-1} range are attributed to the Ti–O stretching vibrations, signaling the incorporation of TiO_2 into the composite [40]. Upon the modification of $Fe_3O_4/SiO_2/TiO_2$ with copper, resulting in the $Fe_3O_4/SiO_2/TiO_2/Cu$ nanocomposite as shown in Fig. 5c, the emergence of a peak at 510 cm^{-1} confirms the formation of the Cu–O bond [41].

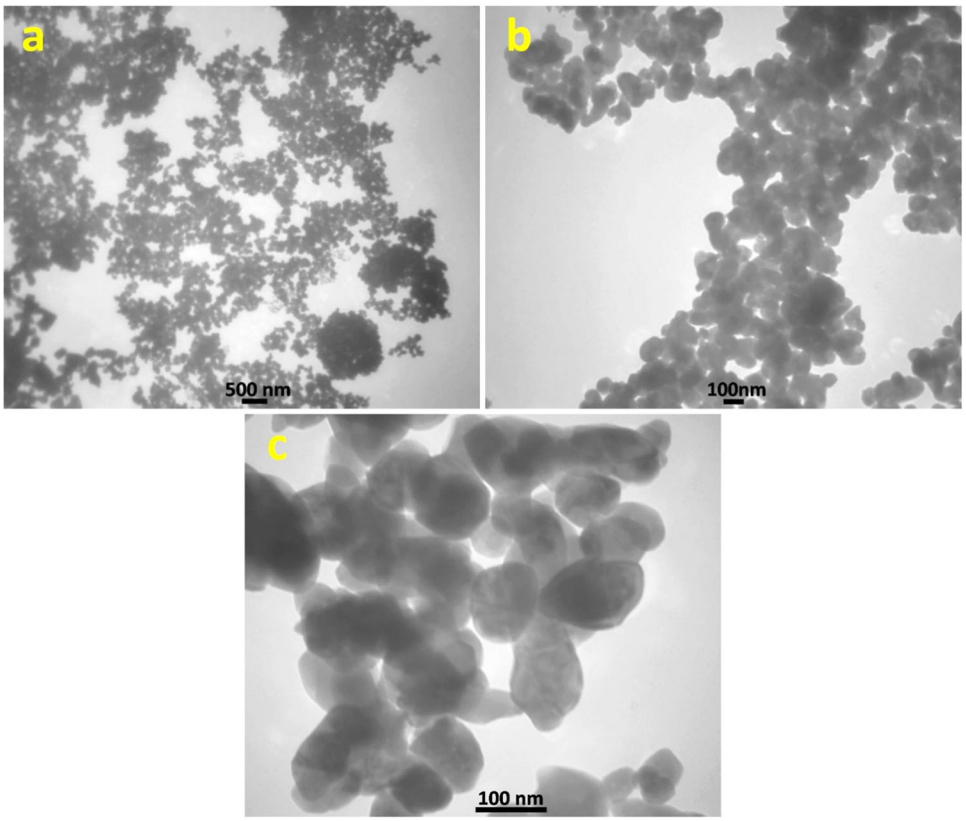

Fig. 4 TEM images of Fe_3O_4/SiO_2/TiO_2/Cu nanocomposite in different magnifications with scale bars at (**a**) 500 nm, (**b**) and (**c**) 100 nm.

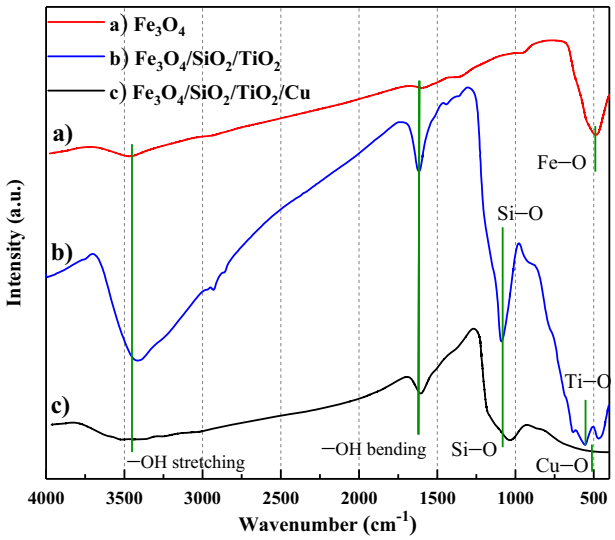

Fig. 5 FT-IR spectrum of (**a**) Fe_3O_4 (**b**) $Fe_3O_4/SiO_2/TiO_2$ and (**c**) $Fe_3O_4/SiO_2/TiO_2$/Cu

Additionally, a notable shift in the Si-O stretching vibration is observed, moving from its typical position to 1028 cm^{-1}. This shift is indicative of changes in the chemical environment surrounding the SiO_2, likely due to the surface modification induced by the incorporation of copper into the nanocomposite [41, 42]. Such a modification could alter the electronic environment of the silicon atoms, leading to a change in the vibrational frequency of the Si-O bonds. This observation further confirms the successful modification of the $Fe_3O_4/SiO_2/TiO_2$ nanocomposite's surface, highlighting the complex interplay of interactions at the nanoscale that contribute to the altered physical and chemical properties of the material. Collectively, these FT-IR spectral features verify the successful synthesis of the nanocomposites and the presence of key chemical bonds corresponding to each component within the materials.

For the measurement of band gap, we use of UV-Vis diffuse reflectance spectrum. If the light of that energy interacts with the material, it is absorbed consequence in an excitation of the electrons from the valence bands into the conduction band. The Tauc plot was drawn according to the Diffuse Reflectance Spectroscopy (DRS) results, which is a graphical representation used in materials science to determine the optical band gap of a semiconductor material. The plot shows $(\alpha h\nu)^2$ versus the photon energy ($h\nu$), where α is the absorption coefficient and $h\nu$ is the photon energy. The determination of the band gap using the Tauc plot involves plotting $(\alpha h\nu)^2$ against the photon energy ($h\nu$), where α is the absorption coefficient. The plot's linear region is extrapolated to the energy axis to determine the optical band gap (E_g) of a direct band gap semiconductor. For indirect band gap materials, $(\alpha h\nu)^{1/2}$ is plotted instead. This method is widely accepted in materials science for estimating the band gap of thin films and nanocomposite materials.

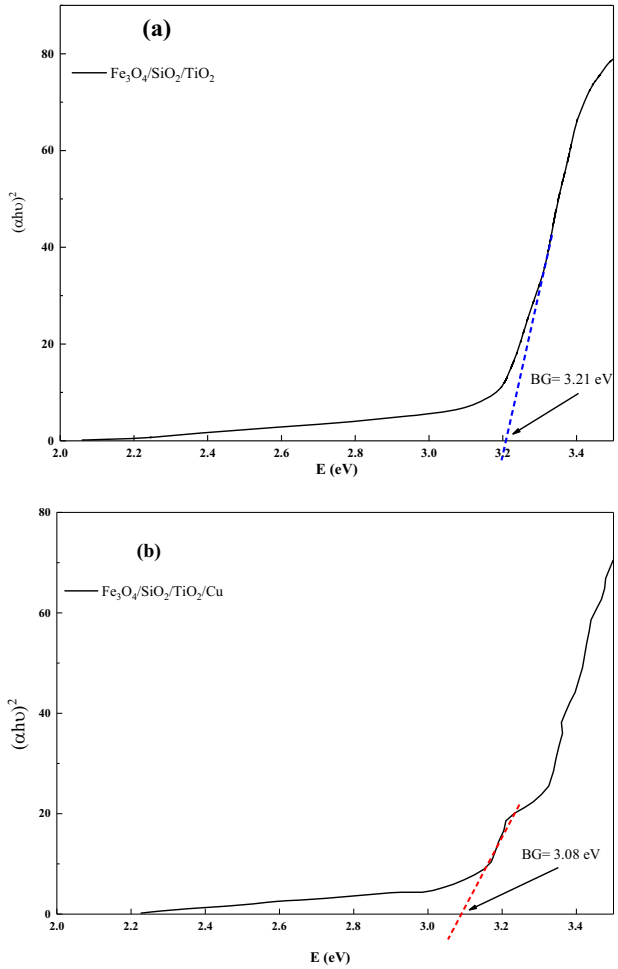

Fig. 6 The calculated band gap for (**a**) $Fe_3O_4/SiO_2/TiO_2$ (**b**) $Fe_3O_4/SiO_2/TiO_2/Cu$

In a Tauc plot, the linear portion of the plot, when extrapolated to the energy axis (where $(\alpha h\nu)^2 = 0$), gives an estimate of the band gap energy of the material. The band gap energy is a critical parameter that defines the energy range in which no electronic states can exist; it is essentially the energy difference between the top of the valence band and the bottom of the conduction band. The approximation band gap value (E_g) was 3.21 eV and 3.08 eV for $Fe_3O_4/SiO_2/TiO_2$ and $Fe_3O_4/SiO_2/TiO_2/Cu$ samples respectively (Fig. 6).

The conduction band edge (E_{CB}) and valence band edge (E_{VB}) of the semiconducting components can be estimated using the formulas [43, 44]:

$$E_{VB} = X - E_e + 0.5\,E_g \quad (1)$$

$$E_{CB} = E_{VB} - E_g \quad (2)$$

where X is the absolute electronegativity of the semiconductor and the band gap energy (E_g) calculated by Tauc plot

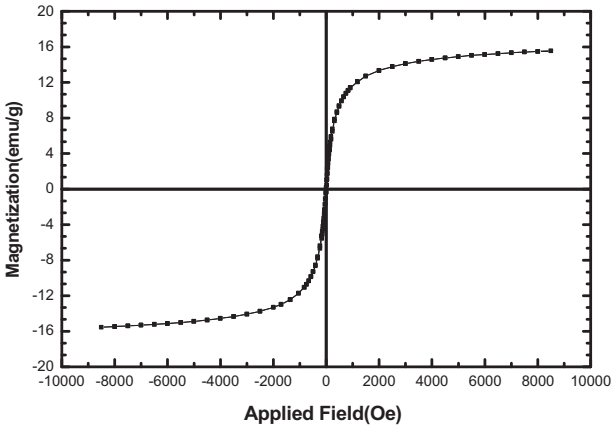

Fig. 7 Vibrating sample magnetometer (VSM) of $Fe_3O_4/SiO_2/TiO_2/Cu$

for the nanocomposite. Based on the provided band gap energy (3.08 eV) for the $Fe_3O_4/SiO_2/TiO_2/Cu$ nanocomposite and the absolute electronegativity (5.81 eV) for TiO_2, the calculated energy band edges by using Eqs. (1) and (2) are as follows:

The Valence Band Edge (E_{VB}) is approximately 2.85 eV.

The Conduction Band Edge (E_{CB}) is approximately −0.23 eV.

The magnetic hysteresis loop of $Fe_3O_4/SiO_2/TiO_2/Cu$ shows its superparamagnetic behavior at room temperature in Fig. 7. The VSM analysis of the $Fe_3O_4/SiO_2/TiO_2/Cu$ nanocomposite would typically show the material's magnetic response to an external field. The saturation magnetization (M_s) is the plateau of the curve, indicating the maximum magnetization Fe_3O_4 can achieve. The coercivity (H_c) is the field strength required to reduce the magnetization to zero, reflecting the material's magnetic hardness. Remanence (M_r) is the residual magnetization after removing the external field. The presence of SiO_2 and TiO_2, which are non-magnetic, along with Cu, which may be paramagnetic or weakly ferromagnetic, can reduce M_s and potentially affect H_c, indicating that the composite's overall magnetic properties are a balance between the magnetic Fe_3O_4 core and the influence of the non-magnetic coatings. The saturation magnetization (Ms) of $Fe_3O_4/SiO_2/TiO_2/Cu$ is 15.74 emu/g. So we can use the external field for separate the nanocatalyst from solution.

The magnetic properties of nanocomposites, specifically the Fe_3O_4 component, play a crucial role in enhancing their separation and recovery from water treatment processes. This is evident in several aspects: Firstly, the presence of Fe_3O_4, a magnetic material, allows for the efficient application of an external magnetic field, which significantly improves the separation of nanocomposites from treated water. This feature is particularly advantageous in continuous flow systems where rapid and effective separation is essential. Secondly, the ease of magnetic separation means that these nanocomposites can be quickly removed, cleaned, and reused in subsequent water treatment cycles, contributing to the sustainability and

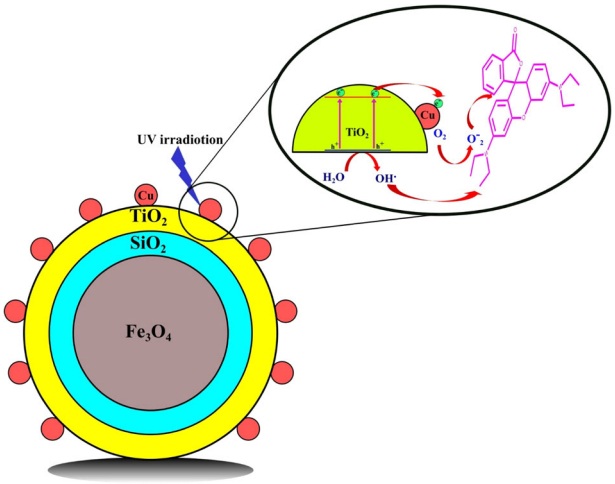

Scheme 2 Mechanism of $Fe_3O_4/SiO_2/TiO_2/Cu$ photocatalysis

cost-effectiveness of the process. Thirdly, magnetic separation offers the advantage of minimizing secondary pollution, as it negates the need for additional chemicals or complex filtration processes that might introduce new contaminants. Finally, the robustness of the magnetic properties under various water treatment conditions, such as fluctuating pH levels or the presence of diverse contaminants, ensures consistent performance of the nanocomposites in a wide range of scenarios, further solidifying their utility in water treatment applications.

The degradation of MB utilizing $Fe_3O_4/SiO_2/TiO_2$ and $Fe_3O_4/SiO_2/TiO_2/Cu$ as photocatalysts under UV irradiation was monitored through UV–Visible spectroscopy, with the results presented in Scheme 2. During this photocatalytic reaction, the absorption of photons whose energy is equal to or surpasses the band gap energy of the photocatalysts results in the excitation of electrons from the valence band to the conduction band, thereby generating electron-hole pairs. Subsequent pathways for these electron-hole pairs are critical to the photocatalytic process. They may recombine, which diminishes photocatalytic efficiency, or they may become trapped in metastable surface states such as Cu^+/Cu. Copper clusters can act as co-catalysts, facilitating the separation of these charge carriers and promoting their involvement in surface reactions. Alternatively, the electron in the conduction band may be captured by electron acceptors like dissolved oxygen molecules, while the hole in the valence band might react with electron donors such as hydroxide ions or water molecules. These interactions lead to the formation of hydroxyl radicals, which can then oxidize and decompose the pollutants [45].

The mechanism of hydroxyl radical production in a TiO_2 and Cu-based photocatalytic system involves several key steps:

$$TiO_2 + hv \rightarrow h^+$$
$$Cu^{2+} + e^- \rightarrow Cu^+$$
$$Cu^+ + e^- \rightarrow Cu$$
$$H_2O + h^+ \rightarrow OH^{\cdot}$$
$$O_2 + e^- \rightarrow O_2^{\cdot -}$$
$$O_2 + Cu^+ \rightarrow Cu^+ + O_2^{\cdot -}$$
$$OH^{\cdot} \text{ or } O_2^{\cdot -} \rightarrow CO_2 + H_2O$$

The photocatalytic mechanism initiates when TiO_2 nanoparticles absorb photons, which prompts the generation of electron-hole pairs on their surface. This photoexcitation event leads to the formation of electrons (e^-) in the conduction band and holes (h^+) in the valence band of the TiO_2. These excited-state charge carriers subsequently interact with the semiconductor's surface and surrounding molecules, as depicted in Scheme 2. Photocatalyst degradation of MB by $Fe_3O_4/SiO_2/TiO_2$ and $Fe_3O_4/SiO_2/TiO_2/Cu$ nanoparticles was accomplished under ultraviolet light irradiation. Degradation Percent of MB in time of t (DP (t)) was calculated as follows:

$$DP(t) = \frac{A_0 - A_t}{A_0} \times 100 \quad (3)$$

Where A_0 absorbance absorbance value of the solution at 0 t and A_t absorbance value at t minute. 200 W Mercury lamps was used as a light source and kept 40 cm away from the photocatalytic quartz tube during the photocatalytic activity measurement [46].

A quantity of 5 mg of the photocatalysts (either $Fe_3O_4/SiO_2/TiO_2$ or $Fe_3O_4/SiO_2/TiO_2/Cu$) was introduced into a 50 mL MB solution with a concentration of 10 mg L^{-1}, contained within a quartz tube. This suspension was subjected to ultrasonication for 15 min to ensure thorough mixing. Subsequently, the mixture was agitated using a magnetic stirrer while being irradiated with UV light at ambient temperature. It was observed that without the application of UV light irradiation, no significant degradation of the dye occurred within 80 min. Upon activation by UV irradiation, the MB dye underwent decomposition, leading to a discernible lightening of the solution's color, culminating at 80 min. Figure 8 illustrates the photocatalytic degradation curves of $Fe_3O_4/SiO_2/TiO_2$ and $Fe_3O_4/SiO_2/TiO_2/Cu$ at room temperature. After a duration of 90 min, the degradation percentage for $Fe_3O_4/SiO_2/TiO_2$ was recorded at 73%, whereas an enhanced degradation percentage of 86% was achieved for $Fe_3O_4/SiO_2/TiO_2/Cu$.

The $Fe_3O_4/SiO_2/TiO_2/Cu$ nanocomposites demonstrated a high efficiency in degrading specific pollutants under light irradiation, a capability attributed to the

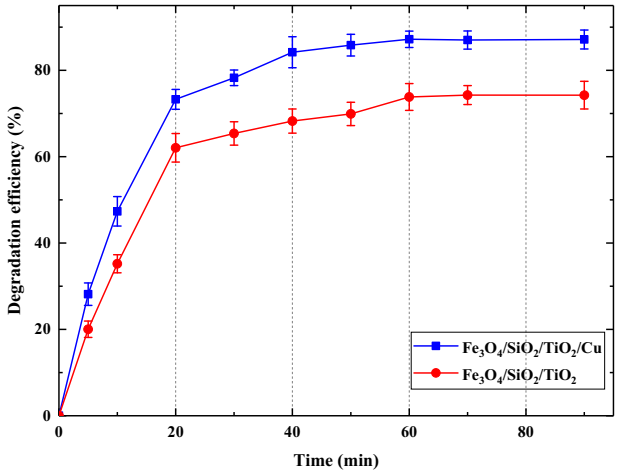

Fig. 8 Photocatalytic degradation curves of Methylene blue (MB) by of $Fe_3O_4/SiO_2/TiO_2$ and of $Fe_3O_4/SiO_2/TiO_2$/Cu under UV irradiation

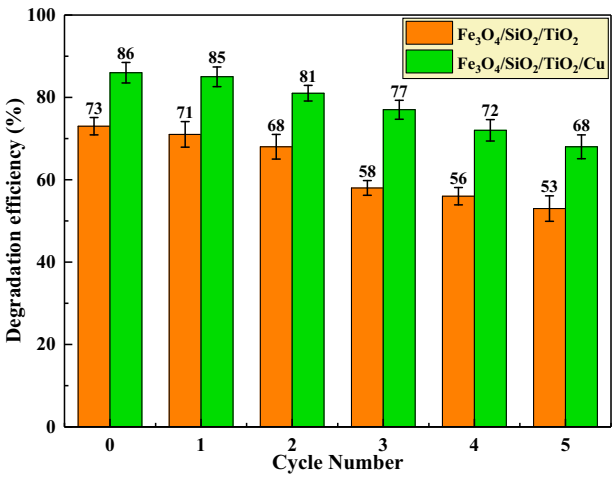

Fig. 9 Photocatalytic performance of $Fe_3O_4/SiO_2/TiO_2$ and $Fe_3O_4/SiO_2/TiO_2$/Cu after 5 recycling times

synergistic action of TiO_2 and Cu in generating reactive oxygen species. This photocatalytic activity, particularly effective under certain light conditions, is crucial for water treatment applications, specifically targeting the breakdown of various organic compounds and dyes commonly found in wastewater.

Actuallt the photocatalytic mechanism of our $Fe_3O_4/SiO_2/TiO_2$/Cu nanocomposite involves several key components working in synergy. Under UV light irradiation, TiO_2 absorbs the light, exciting electrons from the valence band to the conduction band and creating electron-hole pairs. Copper clusters in the nanocomposite act as co-catalysts, enhancing the separation of these charge carriers and facilitating their involvement in surface reactions. The function of Cu as an electron acceptor, and the synergistic interactions that lead to enhanced catalytic performance. This significantly reduces the recombination rate of electron-hole pairs, thereby improving the photocatalytic efficiency.

Following the photocatalytic reaction, the nanoparticles were recovered from the solution utilizing an external magnetic field and were subsequently employed in subsequent cycles. Because the Fe_3O_4 core enables magnetic separation, and the SiO_2 layer provides stability, preventing Fe_3O_4 oxidation. This multifaceted interaction among the components results in a highly efficient system for degrading organic pollutants, making this nanocomposite a promising tool for environmental remediation. The sustained photocatalytic performance of both $Fe_3O_4/SiO_2/TiO_2$ and $Fe_3O_4/SiO_2/TiO_2$/Cu after five recycling iterations is depicted in Fig. 9, where the catalysts demonstrated acceptable efficiency following multiple recovery and reuse cycles.

4 Conclusion

In summary, the magnetically responsive $Fe_3O_4/SiO_2/TiO_2$ nanoparticles were synthesized via the sol-gel technique, while the $Fe_3O_4/SiO_2/TiO_2$/Cu composites were fabricated through a straightforward photodeposition approach. Comprehensive characterization of the structural and morphological features of the magnetic nanoparticles was conducted employing a suite of analytical techniques, including XRD, EDS, Field Emission Scanning Electron Microscopy (FE-SEM), Fourier-Transform Infrared Spectroscopy (FT-IR), DRS, and Vibrating Sample Magnetometry (VSM). TEM analysis revealed that the average size of the $Fe_3O_4/SiO_2/TiO_2$/Cu nanocomposite particles was approximately 75 nm. The $Fe_3O_4/SiO_2/TiO_2$/Cu nanocomposite demonstrated superior photocatalytic performance when subjected to UV irradiation, compared to its counterparts. The significant photocatalytic activity, enhanced chemical stability, and efficient magnetic separability of the $Fe_3O_4/SiO_2/TiO_2$/Cu nanocomposite render it a highly advantageous material for real-world photocatalytic applications.

Acknowledgements We would like to express our sincere gratitude to the Scientific Research Center of *Soran University* for their support and assistance throughout the course of this research project. Their commitment to promoting scientific research and fostering an environment of academic excellence has been instrumental in the successful completion of this study. We extend our appreciation to the staff and faculty members of the Scientific Research Center for their valuable guidance, technical expertize, and access to research facilities. Their contributions have significantly enhanced the quality of our work and have played a crucial role in the achievement of our research goals.

Author contributions HK contributed to the conceptualization of the study, formulation of the research design, and oversight of the entire

research project. NS played a key role in the synthesis and characterization of nanoparticles, including the application of various methods such as sol-gel and precipitation. PA contributed significantly to the experimental work, data collection, and analysis. MPM and SMM were involved in the application phase of the study, specifically in the degradation of organic dye. All authors actively participated in the drafting and critical review of the manuscript. HK and PA were particularly involved in the writing of the original draft, while NS, MPM, and SMM contributed to the manuscript's review and editing process. The final version of the manuscript was approved by all authors.

Compliance with ethical standards

Conflict of interest The authors declare no competing interests.

References

1. Johir M, Vigneswaran S, Kandasamy J, Sleigh R (2013) Coupling of physico-chemical treatment and steel membrane filtration to enhanced organic removal in wastewater treatment. Desalin Water Treat 51(13-15):2695–2701
2. Wang R, Wang X, Xi X, Hu R, Jiang G (2012) Preparation and photocatalytic activity of magnetic $Fe_3O_4/SiO_2/TiO_2$ composites. Adv Mater Sci Eng 2012:409379
3. Xu X, Ji F, Fan Z, He L (2011) Degradation of glyphosate in soil photocatalyzed by $Fe_3O_4/SiO_2/TiO_2$ under solar light. Int J Environ Res Public Health 8(4):1258–1270
4. Chi Y, Yuan Q, Li Y, Zhao L, Li N, Li X, Yan W (2013) Magnetically separable $Fe_3O_4@SiO_2@TiO_2$-Ag microspheres with well-designed nanostructure and enhanced photocatalytic activity. J Hazard Mater 262:404–411
5. Xu J, Wang F, Liu W, Cao W (2013) Nanocrystalline N-doped powders: mild hydrothermal synthesis and photocatalytic degradation of phenol under visible light irradiation. Int J Photoenergy 2013:616139
6. Zheng W, Zou Y, Li X, Machesky ML (2013) Fate of estrogen conjugate 17α-estradiol-3-sulfate in dairy wastewater: comparison of aerobic and anaerobic degradation and metabolite formation. J Hazard Mater 258:109–115
7. Luo X, Zhang S, Lin X (2013) New insights on degradation of methylene blue using thermocatalytic reactions catalyzed by low-temperature excitation. J Hazard Mater 260:112–121
8. Xu Z, Yu J (2011) Visible-light-induced photoelectrochemical behaviors of Fe-modified TiO_2 nanotube arrays. Nanoscale 3(8):3138–3144
9. Wang H, Wu Z, Liu Y (2009) A simple two-step template approach for preparing carbon-doped mesoporous TiO_2 hollow microspheres. J Phys Chem C 113(30):13317–13324
10. Mo J, Zhang Y, Xu Q, Lamson JJ, Zhao R (2009) Photocatalytic purification of volatile organic compounds in indoor air: a literature review. Atmos Environ 43(14):2229–2246
11. Astruc D, Lu F, Aranzaes JR (2005) Nanoparticles as recyclable catalysts: the frontier between homogeneous and heterogeneous catalysis. Angew Chem Int Ed 44(48):7852–7872
12. Phan NT, Jones CW (2006) Highly accessible catalytic sites on recyclable organosilane-functionalized magnetic nanoparticles: an alternative to functionalized porous silica catalysts. J Mol Catal A: Chem 253(1):123–131
13. Liu Z, Bai H, Sun DD (2011) Facile fabrication of porous chitosan/TiO_2/Fe_3O_4 microspheres with multifunction for water purifications. N. J Chem 35(1):137–140
14. Álvarez PM, Jaramillo J, Lopez-Pinero F, Plucinski PK (2010) Preparation and characterization of magnetic TiO_2 nanoparticles and their utilization for the degradation of emerging pollutants in water. Appl Catal B: Environ 100(1):338–345
15. Shokouhimehr M, Piao Y, Kim J, Jang Y, Hyeon T (2007) A magnetically recyclable nanocomposite catalyst for olefin epoxidation. Angew Chem Int Ed 46(37):7039–7043
16. Ovcharov ML, Mishura AM, Granchak VM (2023) Photocatalytic activity of electrochemically formed Ag_2O in the process of CO_2 reduction with water vapor under the effect of visible light. Theor Exp Chem 59(2):112–119. https://doi.org/10.1007/s11237-023-09770-9
17. Sachuk OV, Zazhigalov VA, Kiziun OV, Hes NL, Mylin AM, Kotynska LY, Kuznetsova LS, Shcherbakov SM, Kordan VM (2022) Influence of mechanochemical and sonochemical methods of preparation of TiO_2/ZrO_2 composites on photocatalytic performance in prometrine decomposition. Theor Exp Chem 58(3):190–197. https://doi.org/10.1007/s11237-022-09735-4
18. Zhuang H, Xia H, Zhang T, Xiao D (2008) Synthesis, characterization, and visible-light photocatalytic activity of Fe2O3/SnO2 nanocomposites. Mater Sci–Pol 26:517–526
19. Serpone N, Maruthamuthu P, Pichat P, Pelizzetti E, Hidaka H (1995) Exploiting the interparticle electron transfer process in the photocatalysed oxidation of phenol, 2-chlorophenol and pentachlorophenol: chemical evidence for electron and hole transfer between coupled semiconductors. J Photochem Photobiol A: Chem 85(3):247–255
20. Zhang H, Wu X, Wang Y, Chen X, Li Z, Yu T, Ye J, Zou Z (2007) Preparation of $Fe_2O_3/SrTiO_3$ composite powders and their photocatalytic properties. J Phys Chem Solids 68(2):280–283
21. Xu F, Volkov V, Zhu Y, Bai H, Rea A, Valappil NV, Su W, Gao X, Kuskovsky IL, Matsui H (2009) Long electron− hole separation of ZnO-CdS core− shell quantum dots. J Phys Chem C 113(45):19419–19423
22. Jing L, Xu Z, Sun X, Shang J, Cai W (2001) The surface properties and photocatalytic activities of ZnO ultrafine particles. Appl Surf Sci 180(3):308–314
23. Cun W, Jincai Z, Xinming W, Bixian M, Guoying S, Ping'an P, Jiamo F (2002) Preparation, characterization and photocatalytic activity of nano-sized ZnO/SnO_2 coupled photocatalysts. Appl Catal B: Environ 39(3):269–279
24. Mohammadi-Aghdam S, Mizwari ZM, Khojasteh H (2023) Visible light photoactivity of the Cu doped TiO_2/Yb_2O_3 nanocomposite for degradation of acid red 88 solution. J Sol-Gel Sci Technol 108(1):127–135
25. Batool T, Shah ZH, Ashraf H, Ali D, Shamaila S, Anjum T, Naseem S, Riaz S (2023) Solar energy driven photo catalytic action and antimicrobial activities of Iron oxide nanoparticles. J Sol-Gel Sci Technol 108(3):655–671. https://doi.org/10.1007/s10971-023-06210-x
26. Zhian H, Khojasteh H, Azimi C (2023) Eco-friendly hydrothermal synthesis of CuO nanoparticles using natural materials as reducing and capping agents. Iran J Chem Chem Eng. https://doi.org/10.30492/ijcce.2023.2002779.6038
27. Abbasi A, Khojasteh H, Keihan AH, Adib K, Sobhani-Nasab A, Rahimi-Nasrabadi M (2021) Co-precipitation synthesis of Ag-doped $NiCr_2O_4$ nanoparticles: investigation of structural, optical, magnetic, and photocatalytic properties. J Mater Sci: Mater Electron 32:1413–1426
28. Safajou H, Ghanbari M, Amiri O, Khojasteh H, Namvar F, Zinatloo-Ajabshir S, Salavati-Niasari M (2021) Green synthesis and characterization of RGO/Cu nanocomposites as photocatalytic degradation of organic pollutants in waste-water. Int J Hydrog Energy 46(39):20534–20546
29. Xiang S, Khan A, Zhou Z, He B, Wang X, Wang B, Weng Q (2022) Photocatalytic hydrogen evolution from water based on

Zn–terpyridine 2D coordination nanosheets. J Mater Chem A 10(45):24345–24352. https://doi.org/10.1039/D2TA05114A
30. Guo S, Li X, Li J, Wei B (2021) Boosting photocatalytic hydrogen production from water by photothermally induced biphase systems. Nat Commun 12(1):1343. https://doi.org/10.1038/s41467-021-21526-4
31. Chen X, Zhao J, Li G, Zhang D, Li H (2022) Recent advances in photocatalytic renewable energy production. Energy Mater. https://doi.org/10.20517/energymater.2021.24
32. Rafiq A, Ikram M, Ali S, Niaz F, Khan M, Khan Q, Maqbool M (2021) Photocatalytic degradation of dyes using semiconductor photocatalysts to clean industrial water pollution. J Ind Eng Chem 97:111–128. https://doi.org/10.1016/j.jiec.2021.02.017
33. Opeida IA, Kytsya AR, Bazylyak LI, Pobigun-Halaiska OI (2018) Magnetically separable nanocatalyst Ag@Ni for the liquid-phase oxidation of cumene. Theor Exp Chem 54(4):242–246. https://doi.org/10.1007/s11237-018-9569-3
34. Yirga G, Bekele H (2019) Synthesis and characterization of humic acid-coated Fe_3O_4 nanoparticles for methylene blue adsorption activity. Adv Mater Lett. https://doi.org/10.5185/amlett.2019.0049
35. Malega F, Indrayana IPT, Suharyadi E (2018) Synthesis and characterization of the microstructure and functional group bond of Fe3o4 nanoparticles from natural iron sand in Tobelo North Halmahera. J Ilm Pendidik Fis Al-Biruni. https://doi.org/10.24042/jipfalbiruni.v7i2.2913
36. Naghani ME, Neghabi M, Zadsar M, Ahangar HA (2023) Synthesis and characterization of linear/nonlinear optical properties of graphene oxide and reduced graphene oxide-based zinc oxide nanocomposite. Sci Rep. https://doi.org/10.1038/s41598-023-28307-7
37. Wang H, Grant DJ, Burns PC, Na C (2015) Infrared signature of the cation−π Interaction Between Calcite and Aromatic Hydrocarbons. Langmuir. https://doi.org/10.1021/acs.langmuir.5b00610
38. Ibrahim M, Amer MA, Ibrahim HAH, Zaghloul EH (2022) Considerable production of ulvan from ulva lactuca with special emphasis on its antimicrobial and anti-fouling properties. Appl Biochem Biotechnol. https://doi.org/10.1007/s12010-022-03867-y
39. Seroka NS, Taziwa R, Khotseng L (2022) Green synthesis of crystalline silica from sugarcane bagasse ash: physico-chemical properties. Nanomaterials 12(13):2184
40. Indrawati D, Syarif N, Rohendi D (2021) Synthesis and characterization of amorphous tio2 anode prepared by anodizing method for na-ion batteries. Indones J Fundam Appl Chem. https://doi.org/10.24845/ijfac.v6.i1.20
41. İpek B, Wulfers MJ, Kim H, Göltl F, Hermans I, Smith JP, Booksh KS, Brown CM, Lobo RF (2017) Formation of formation of $[Cu_2O_2]^{2+}$ and $[Cu_2O]^{2+}$ toward C–H bond activation in Cu-SSZ-13 and Cu-SSZ-39. ACS Catal. https://doi.org/10.1021/acscatal.6b03005
42. Świsłocka R (2010) Comparison of molecular structure of alkali metal ortho substituted benzoates. Spectrosc Int J. https://doi.org/10.1155/2010/848967
43. Kampalapura Swamy C, Hezam A, Mavinakere Ramesh A, Habbanakuppe Ramakrishnegowda D, K. Purushothama D, Krishnegowda J, Kanchugarakoppal SR, Shivanna S (2021) Microwave hydrothermal synthesis of copper induced ZnO/gC_3N_4 heterostructure with efficient photocatalytic degradation through S-scheme mechanism. J Photochem Photobiol A: Chem 418:113394. https://doi.org/10.1016/j.jphotochem.2021.113394
44. Saleem MZ, Nadeem N, Shahbaz M, Al-Zaqri N, Rasul S, Noreen S, Zahid M, shahid I (2023) Coal fly ash supported $Ag@Bi_2WO_6$: a novel heterogeneous nanocomposite for effective sunlight driven photocatalytic degradation of dye. Phys Chem Earth, Parts A/B/C 132:103506. https://doi.org/10.1016/j.pce.2023.103506
45. Kramar AS, Malysheva ML, Anishchenko VM, Kuzema PO, Stavinskaya OM, Smirnova NP, Laguta IV, Ivannikov RV, Linnik OP (2023) Photocatalytic conversion of lignin in the presence of titania and iron titanate films. Theor Exp Chem 59(3):178–185. https://doi.org/10.1007/s11237-023-09776-3
46. Abbasi A, Keihan AH, Ahmadi Golsefidi M, Rahimi-Nasrabadi M, Khojasteh H (2020) Synthesis, characterization and photocatalytic activity of $FeCr_2O_4$ and $FeCr_2O_4$/Ag nanocomposites. J Nanostruct 10(3):518–530. https://doi.org/10.22052/jns.2020.03.008